Supplementary Information for

Spectral-acoustic-coordinated astigmatic metalens for wide field-of-view and high-speed spatiotemporal 3D imaging

Shujian Gong[1,2,3†], Yinghui Guo[1,2,3,4†], Xiaoyin Li[1,2†], Mingbo Pu[1,2,3,4*], Peng Tian[1,2], Qi Zhang[1,2], Lianwei Chen[1,2], Wenyi Ye[1,2,3], Heping Liu[5], Fei Zhang[1,2], Mingfeng Xu[1,2], and Xiangang Luo[1,2,3*]

[1]State Key Laboratory of Optical Field Manipulation Science and Technology, Institute of Optics and Electronics, Chinese Academy of Sciences, Chengdu 610209, China.
[2]Research Center on Vector Optical Fields, Institute of Optics and Electronics, Chinese Academy of Sciences, Chengdu 610209, China.
[3]College of Materials Sciences and Opto-Electronic Technology, University of Chinese Academy of Sciences, Beijing 100049, China.
[4]Sichuan Provincial Engineering Research Center of Digital Materials, Chengdu, 610213, China.
[5]Tianfu Xinglong Lake Laboratory, Chengdu, 610213, China.
†These authors contributed equally to this work.
*Email: pmb@ioe.ac.cn, lxg@ioe.ac.cn

This file includes:

Other supporting materials for this manuscript include the following:

Movie S1: Dynamic 3D imaging of a high-speed rotating fan in the *xy*-plane.
(Parameters: AOD scan points: 20 × 83; full-field scan points: 20 × 83 × 30; frame rate: 183.5 fps at $\beta = 4$, 367 fps at $\beta = 2$, and 734 fps at $\beta = 1$)

Movie S2: Dynamic 3D imaging of two rotating cylindrical targets in the *xz*-plane.
(Parameters: AOD scan points: 20 × 83; full-field scan points: 20 × 83 × 30; frame rate: 122.3 fps at $\beta = 6$)

Movie S3: Dynamic 3D imaging of a 3kHz chopper.
(Parameters: AOD scan points: 1 × 60; full-field scan points: 1 × 60 × 30; frame rate: 20.3×10^3 fps at $\beta = 1$ and 10.2×10^3 fps at $\beta = 2$)

Supplementary Section 1: Comparisons among related single-channel LiDARs.

Table S1 | Comparison of the performance metrics of similar single-channel transceiver LiDAR systems.

Ref.	Scanning manner	PPAR (MHz)	β (fast axis line rate / slow axis point rate)	FPAR (MHz)	fast axis FOV	fast axis angular resolution θ	$C_{spatial\text{-}1D}$ (rad) (**)
This work	Spectral scanning + 2-axisAOD	36.56	1	36.56	102°	~0.37°	487.6
Ref.[1]	Spectral scanning + Mechanical scanning	30	50 (*)	~0.6	7°	~0.23°	3.67
		88	17 (*)	~5.12	9°	~0.04°	40.2
Ref.[2]	2-axis AOD	6.25	1	6.25	150°	~1.8°	217.3
Ref.[3]	Spectral scanning + Mechanical scanning	21.38	24 (*)	~0.9	2°	~0.044°	1.57
Ref.[4]	Spectral scanning + Mechanical scanning	7.6	1	7.6	7.1°	~0.015°	58.9
Ref.[5]	Spectral scanning + Mechanical scanning	4.1	96	~0.04	2°	~0.04°	1.78
Ref.[6]	Spectral scanning + Mechanical scanning	5.6	1000	~0.0056	~2°	~0.06°	1.95

(*) If not mentioned in the text, the mechanical scanning is calculated based on a maximum point scanning rate of 20 kHz.

(**) Calculated by the fast axis ($C_{spatial\text{-}1D} = N \cdot FOV = FOV^2/\theta$).

Table S1 and Fig. S1 present a comparison of the performance metrics of similar single-channel transceiver LiDAR systems. These systems typically face one or more limitations: some suffer from a narrow FOV (Refs.[1, 3-6]), some experience rate mismatching that results in FPAR dropping below PPAR (Refs.[1, 3-6]), and some encounter beam divergence that reduces the number of resolvable points (Ref.[2]). Taken together, these issues lead to suboptimal comprehensive spatiotemporal detection capabilities.

In contrast, in this work, we first improve the FPAR through rate matching enabled by spectral-acousto-optic (spectral-AO) scanning. Then, to address the FOV mismatch in heterogeneous dual-axis cascade scanning, we uniquely design an astigmatic metalens (AML) to correct beam astigmatism and field distortion caused by spectral-AO scanning, while simultaneously expanding the FOV. This approach ultimately enables exceptional comprehensive spatiotemporal detection capability.

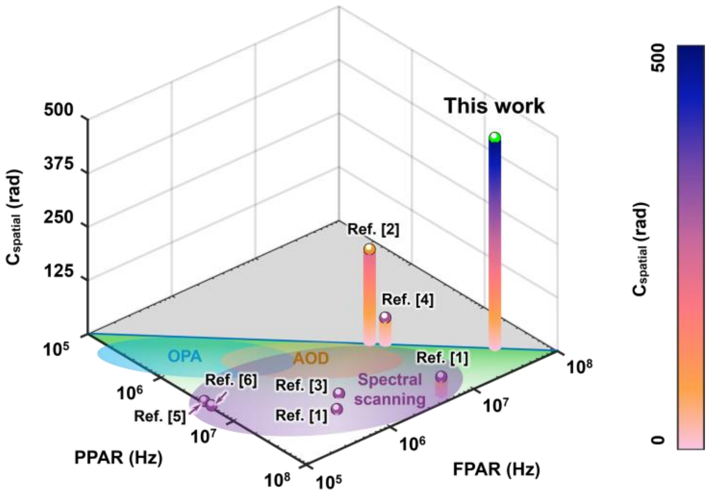

Fig. S1 | Comparison of this work with related studies. The three coordinate axes represent PPAR, FPAR, and spatial detection capability ($C_{spatial\text{-}1D}$). This work achieves both high FPAR and $C_{spatial\text{-}1D}$, demonstrating superior spatiotemporal detection capabilities.

Supplementary Section 2: Low-crosstalk time-frequency multiplexing enabled by programmable spectral shaping.

Figure S2 provides a detailed illustration of how the spectro-temporal encoding module achieves time-frequency multiplexing through time-stretching. Fig. S2a depicts the specific experimental setup, which mainly consists of a pair of arrayed waveguide gratings (AWGs), 30 variable optical attenuators (VOAs) for balancing the output power, and 30 single-mode fibers for time-stretching. AWG1 demultiplexes (DeMUX) the input broadband laser source, producing 30 spectral channels with equal wavelength spacing. In an ideal scenario, these 30 channels transmit through fibers of lengths in an arithmetic progression and are subsequently combined by AWG2, functioning as a wavelength division multiplexer (MUX). This results in the output of discrete chirped pulse sequences with perfectly equal temporal intervals ($\Delta\tau = 24.6$ ns) and equal wavelength spacing ($\Delta\lambda$). Based on this, we can calculate the required common difference in fiber length (ΔL):

$$\Delta L = \frac{c}{n_{eff}} \cdot \Delta\tau \approx 5.03\text{m} \tag{S1}$$

where c denotes the speed of light in vacuum and n_{eff} represents the effective refractive index of the fiber core. To ensure accurate time-of-flight (TOF) calculations, we calibrate the delay times of the 30 time-stretched sub-pulses by detecting the encoding module's output signal, using the laser pulse as a timing reference, as shown in Fig. S2b. The horizontal axis represents the channel number, where channel No. 1 (Ch #1) corresponds to λ = 1541.7 nm and channel No. 30 (Ch #30) corresponds to λ = 1553.3 nm. Fig. S2b(i) shows that the delay times across channels increase almost linearly, consistent with expectations. Fig. S2b(ii) displays the pulse intervals between adjacent channels. Due to deviations in fiber length differences (ΔL) from preset values, the intervals are non-uniform, with the minimum value (~23.4 ns) slightly lower than the average (~24.6 ns).

In our experiment, the laser source generates a supercontinuum spectrum spanning 500-2000 nm, which more than adequately covers the operational wavelength range of 1541-1554 nm, as illustrated in Fig. S2c(i). The total output spectrum after time-stretching is presented in Fig. S2c(ii). The AWG splits the original signal into 30 channels with a wavelength interval of $\Delta\lambda = 0.4$ nm. Although these channels are temporally separated through time-stretching, each channel exhibits a 3 dB bandwidth of 0.28 nm, leading to some spectral overlap and crosstalk between adjacent channels (as shown in the inset of Fig. S2c(ii)). This spectral overlap degrades the spectral resolution and, consequently, reduces the spatial resolution along the horizontal direction after grating dispersion.

To address this issue, we introduced a programmable spectral shaping device known as a Waveshaper (WS), a passive optical component capable of arbitrarily modifying the spectral profile of incident light. In our setup, the WS was configured to perform spectral-domain filtering in a comb-like pattern, with each comb tooth centered at the wavelength corresponding to the 30 channels of the AWG, and a linewidth of 0.13 nm. This configuration allows each channel from the AWG to undergo narrowband filtering through the WS, while also enabling uniform channel intensities via differential spectral attenuation. Fig. S2c(iii) illustrates the spectrum after time-stretching and subsequent WS filtering. Compared to the AWG output spectrum shown in Fig. S2c(ii), the channels exhibit narrower linewidths with reduced crosstalk, thereby significantly enhancing the spatial resolution in the grating's dispersion direction.

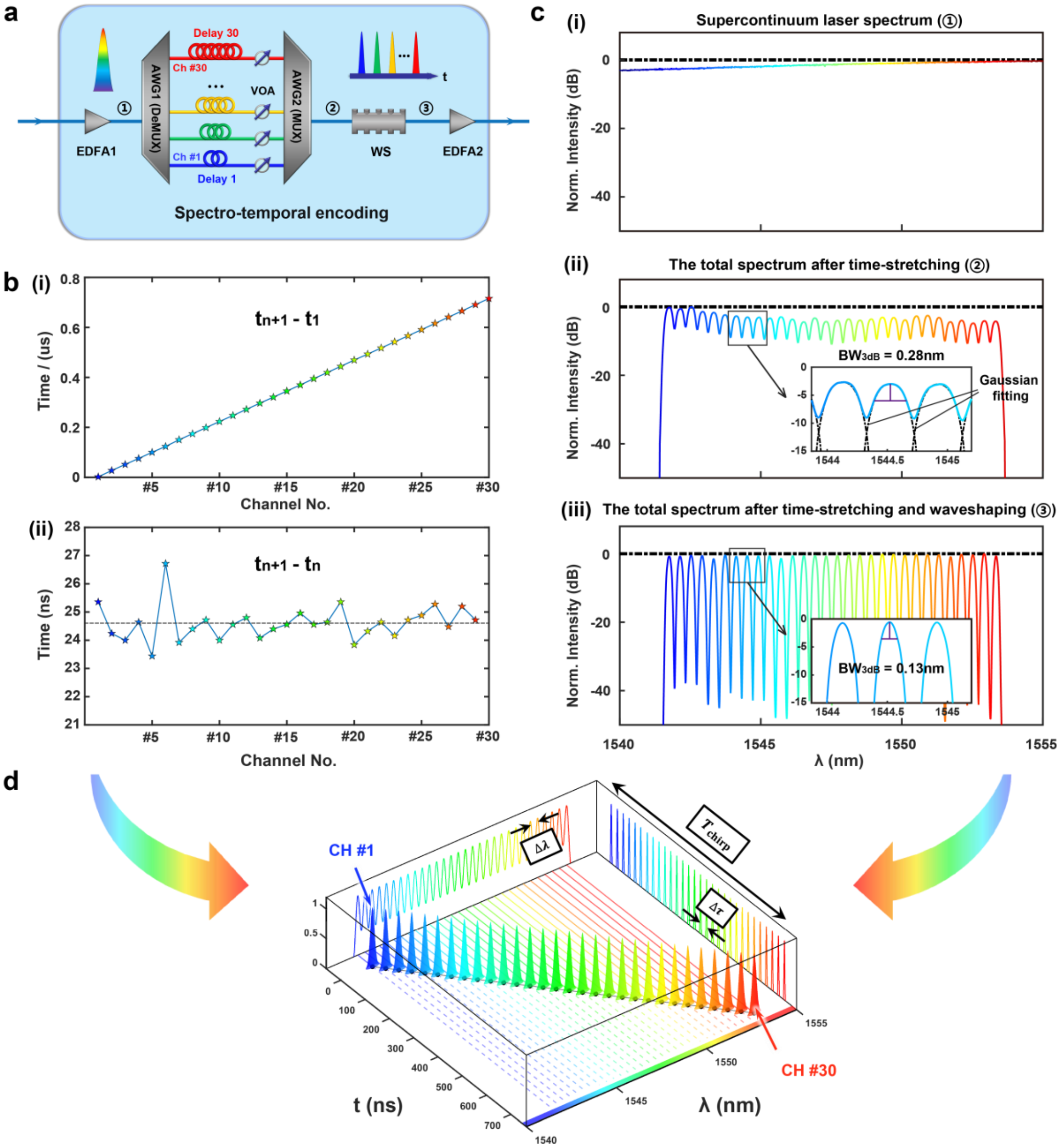

Fig. S2 | Implementation of time-frequency multiplexing. (**a**) Spectro-temporal encoding module. It primarily consists of two arrayed waveguide gratings (AWGs) and several fibers. The AWGs split the source into 30 channels with equal spectral intervals and then combine them. Each channel propagates through fibers of increasing lengths, resulting in time-stretched time-frequency mapping depicted by (**d**). (EDFA: erbium-doped fiber amplifier; VOA: variable optical attenuator; WS: waveshaper). (**b**) (i) Relative time delay of the emitted pulses compared to the first channel (Ch #1); (ii) Relative time delay between emitted pulses of adjacent channels. (**c**) Spectral variations at each stage of time-frequency multiplexing: (i) Spectrum of the incident laser source; (ii) Total spectrum of the 30 channels after time-stretching. The inset shows spectral overlap between adjacent channels; (iii) Total spectrum after time-stretching and waveshaping. The inset shows significant suppression of channel crosstalk. (**d**) The achieved time-frequency mapping features an equal time interval of $\Delta\tau$ between adjacent channels and a total chirped pulse sequence duration of T_{chirp}.

Supplementary Section 3: Spectral-acousto-optic scanning cascading the AML.

The schematic diagram of the spectral-AO cascade scanning is illustrated in Fig. S3a, with the corresponding scanning timing diagram presented in Fig. S3c. The scanning angles of the dual-axis AOD (AA Opto-electronic, DTSXY-A6-1550) are governed by the acousto-optic (AO) Bragg diffraction mechanism. Tuning the driving frequency of the *x*/*y* AOD from 41 to 59 MHz yields the output angles $\Theta_{x,y\text{AOD}} \in [-1.227°, 1.227°]$.

Since the vertically oriented grating only provides spatial dispersion in the horizontal direction, the beam propagation in the two directions will not be symmetric. In the vertical plane (*yz* plane) depicted by Fig. S3d, the scanning direction of *y*AOD is parallel to the orientation of the blazed grating (BG), causing the grating to merely function as a reflective mirror, resulting in an output angle $\Theta_{y\text{BG}} = \Theta_{y\text{AOD}} \in [-1.227°, 1.227°]$. In the horizontal plane (*xz* plane) depicted by Fig. S3e, the scanning direction of *x*AOD is orthogonal to the BG's orientation, resulting in spatial dispersion with an angle extension of $\Theta_{x\text{BG}} \in [-3.95°, 3.95°]$, calculated by the grating equation:

$$\Theta_o = \arcsin\left(\frac{\lambda_n}{d} - \sin\Theta_{i\_xn}\right) \tag{S2}$$

$$\Theta_{xBG} = \Theta_o(\lambda_n, \Theta_{i\_xn}) - \overline{\Theta_o} \tag{S3}$$

where λ_n is the wavelength of the incident light, n = 1, 2, 3, …, 30 denotes the channel number, and d is the grating constant (1/600 mm). The angle Θ_{i_xn} represents the incident angle at the grating and also corresponds to the *x*AOD's output angle at its *xn*-th scanning position, while Θ_o is the diffracted angle of BG. Eq. (S3) is used to reference the angle 0° because the optical axis also shifts upon diffraction. Moreover, Eq. (S2) reveals a nonlinear relationship between the output angle and both the incident angle and wavelength, leading to the slight asymmetry of the horizontal output angle of the BG, as shown in Fig. S3b(i).

Based on Eq. (S3), we can determine the output angle for *x*AOD and the corresponding driving frequencies $f_{x\text{AOD}}$ to ensure that adjacent spectral scanning fields in the horizontal direction connect seamlessly without gaps, expressed as:

$$\Theta_o(\lambda_{30}, \Theta_{i\_x(n)}) \approx \Theta_o(\lambda_1, \Theta_{i\_x(n+1)}) \tag{S4}$$

which derives 7 *x*AOD scanning positions $f_{x\text{AOD}}$ = 41, 44, 47, …, 59 MHz, as illustrated in Fig. S3b(i). Here, $\Delta f_{y\text{AOD}}$ = 0.244 MHz yields 83 scanning positions; combined with 30 spectral channels, this provides a total of 20×83×30 scanning positions. Additionally, for finer scanning, we set $\Delta f_{x\text{AOD}}$ = 0.94 MHz and $\Delta f_{y\text{AOD}}$ = 0.122 MHz, resulting in a denser subpixel scanning lattice, as shown in Fig. S3b(ii).

Consequently, due to horizontal dispersion, the BG's output forms a rectangular FOV. Thus, the designed wide-FOV metalens also requires a phase profile over a rectangular area to match the scanning spot formed after focusing by the front lens.

The angular magnification of such a system resembling a Galileo telescope is given by $M = |f_L / f_{\text{AML}}|$. Since the effective focal length f_{AML} of the AML is limited by the periodicity of the meta-atoms, a longer focal length f_L for the focusing lens is preferable. However, with the maximum size of the AML set at r_{m} = 5 mm, it is crucial to ensure that the focused light spot falls within its effective area while leaving some margin:

$$\sqrt{x_m^2 + y_m^2} \approx f_L \cdot \sqrt{\tan^2\Theta_{xBG\max} + \tan^2\Theta_{yBG\max}} < 0.9 \cdot r_m \tag{S5}$$

where x_{m} and y_{m} represent the coordinates of the edges of the rectangular scanning area. This leads to the condition f_L < 62 mm, prompting us to select f_L = 60 mm (LBTEK, MBCX10611) to maximize the angular magnification. Next, we optimize the phase distribution of the AML using commercial software (Zemax OpticStudio) to achieve a larger horizontal FOV while effectively suppressing beam divergence. The optimized phase profile, expressed by Eq. (8) in the main text, is shown in Fig. 3b, with the corresponding phase coefficients listed in Table S2.

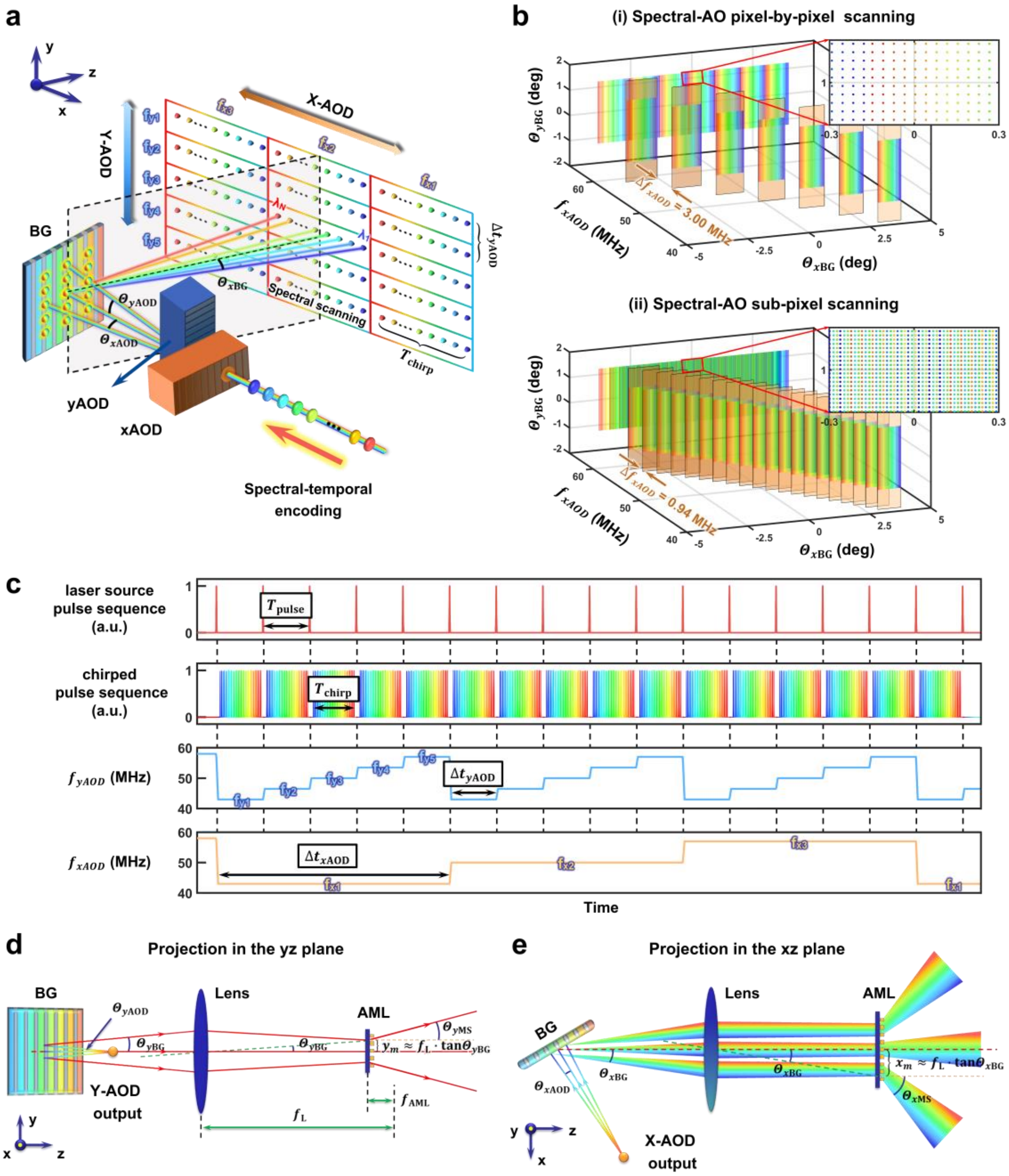

Fig. S3 | Spectral-acousto-optic scanning cascading the AML. (**a**) Schematic of the spectral dual-AO cascade scanning. (**b**) Implementation of (i) pixel-by-pixel scanning and (ii) sub-pixel scanning in spectral-AO scanning. (**c**) Timing diagrams of spectral-dual-AO scanning corresponding to **a**. As an example, consider a complete scan frame comprising 5 *y*AOD and 3 *x*AOD scanning positions. After completing a spectral scan, the *y*AOD swiftly transitions to the next position to achieve rate matching (within the time gap T_{pulse}-T_{chirp}), while the *x*AOD operates in a similar manner. (**d**)(**e**) Schematic of the AML extending the FOV in two orthogonal directions. (**d**) In the *yz*-plane, the BG acts as a planar mirror, with the vertical FOV extending solely through the AML. (**e**) In the *xz*-plane, the BG introduces spatial dispersion that extends the initial horizontal FOV, which is further magnified by the combination of the lens and AML, functioning similarly to a Galilean telescope.

Table S2 | Phase coefficients of the AML.

c_1	c_2	c_3	c_4	c_5	c_6	c_7	c_8	c_9
10070	8099.4	-712.23	403.15	1200.0	260.88	320.00	320.00	320.00

The above coefficients represent the asymmetric modulation in the x and y directions, which reflect the astigmatic characteristics of the AML. By following the standard form of the non-astigmatic defocus phase $\Phi(r) = k_0 r^2/2f$, where $k_0 = 2\pi/\lambda$, the effective focal lengths of the AML in the x/y direction, $f_{\mathrm{AML}\_x,y}$, can be approximately derived as:

$$f_{AML\_x} \approx \frac{\pi r_m^2}{c_1\lambda} = 5.0\mathrm{mm}\ ,\ f_{AML\_y} \approx \frac{\pi r_m^2}{c_2\lambda} = 6.2\mathrm{mm} \quad \text{(S6)}$$

Based on their ratios with f_L, the angular magnification M is ~12-fold/10-fold in the x/y direction relative to the BG's output angles. These values agree closely with the simulated output angles $\Theta_{x\mathrm{AML}} \in [-51°, 51°]$ and $\Theta_{y\mathrm{AML}} \in [-13°, 13°]$ (see Fig. 3c in the main text), with discrepancies mainly arising from higher-order phase modulation at the FOV edges.

Supplementary Section 4: Design of metalens unit cells.

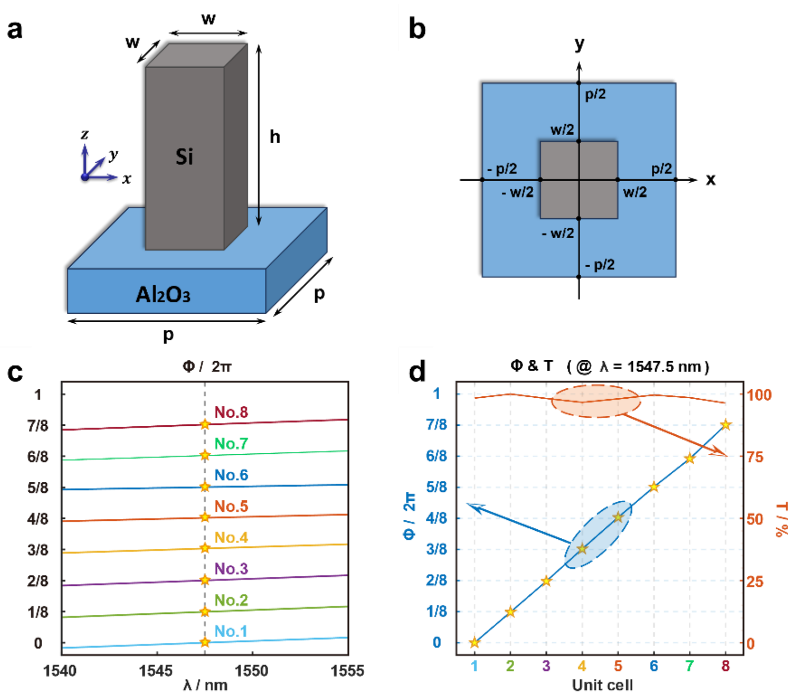

Fig. S4 | Metalens unit cell design at the operational wavelength. (**a**) 3D and (**b**) top-view schematics of the unit cell. The nanopillars and substrate are composed of silicon (Si) and sapphire (Al_2O_3), respectively. Fixed structural parameters: height h = 800 nm and lattice constant p = 651 nm. (**c**) Simulated phase responses of 8 unit cells across the operational wavelength range of 1540-1555 nm. (**d**) Simulated phases and transmissivities of the 8 unit cells at the center wavelength of 1547.5 nm.

The unit cell is a silicon-on-sapphire (SOS) square nanopillar, with the Si nanopillar centered within the cell, as illustrated in Fig. S4a and b. Using the finite-difference time-domain (FDTD) method implemented in Lumerical for simulations, we optimized the structural parameters to yield 8 distinct unit cells, each exhibiting a unique phase response, as shown in Fig. S4c and d. The nanopillar widths (w) for units 1-8 are 222, 268, 293, 313, 332, 354, 382, and 485 nm, respectively. The minimum feature size, calculated as $p - w_{\max}$, is 166 nm, which is compatible with standard micro- and nanofabrication techniques.

Supplementary Section 5: Characterization of the beam deflection angle and FOV.

1. Characterization of beam deflection angle deviations

To validate the expanded FOV capability of the designed AML, we characterized the deviations between the measured and theoretical values of the system's output beam deflection angles:

$$\Delta\Theta_{x,y} = \Theta_{x,y}\left(\text{meas.}\right) - \Theta_{x,y}\left(\text{theo.}\right) \tag{S7}$$

where $\Theta_{x/y}$ (meas.) and $\Theta_{x/y}$ (theo.) denote the measured and theoretical beam deflection angles in the x/y directions, respectively. The measured values were obtained by performing far-field spot position measurements at specific scanning positions, where a small reflector was moved to identify the location with the strongest echo signal. From this, the beam's azimuthal angles were calculated relative to the AML. The theoretical values were derived from the beam emission angles obtained through ZEMAX simulations.

For x/yAOD scanning points of 20 and 83, respectively ($\Delta f_{x\text{AOD}}$ = 0.94 MHz, $\Delta f_{y\text{AOD}}$ = 0.244 MHz), we measured the output angles Θ_x and Θ_y under varying scanning positions: $N_{x\text{AOD}}$: #1, #4, #7, #9, #12, #14, #17, #20; $N_{y\text{AOD}}$: #1, #21, #42, #63, #83; N_λ : #4, #15, #27. This resulted in a total of 8×5×3×2 datasets. The deviations from theoretical values, $\Delta\Theta_x$ and $\Delta\Theta_y$, are illustrated in Fig. S5a (i)-(iii) and b(i)-(iii). By performing linear fitting on these datasets, we determined the deviations across all scanning points and subsequently corrected the actual beam scanning angles, as shown in Fig. S5a (iv) and b (iv).

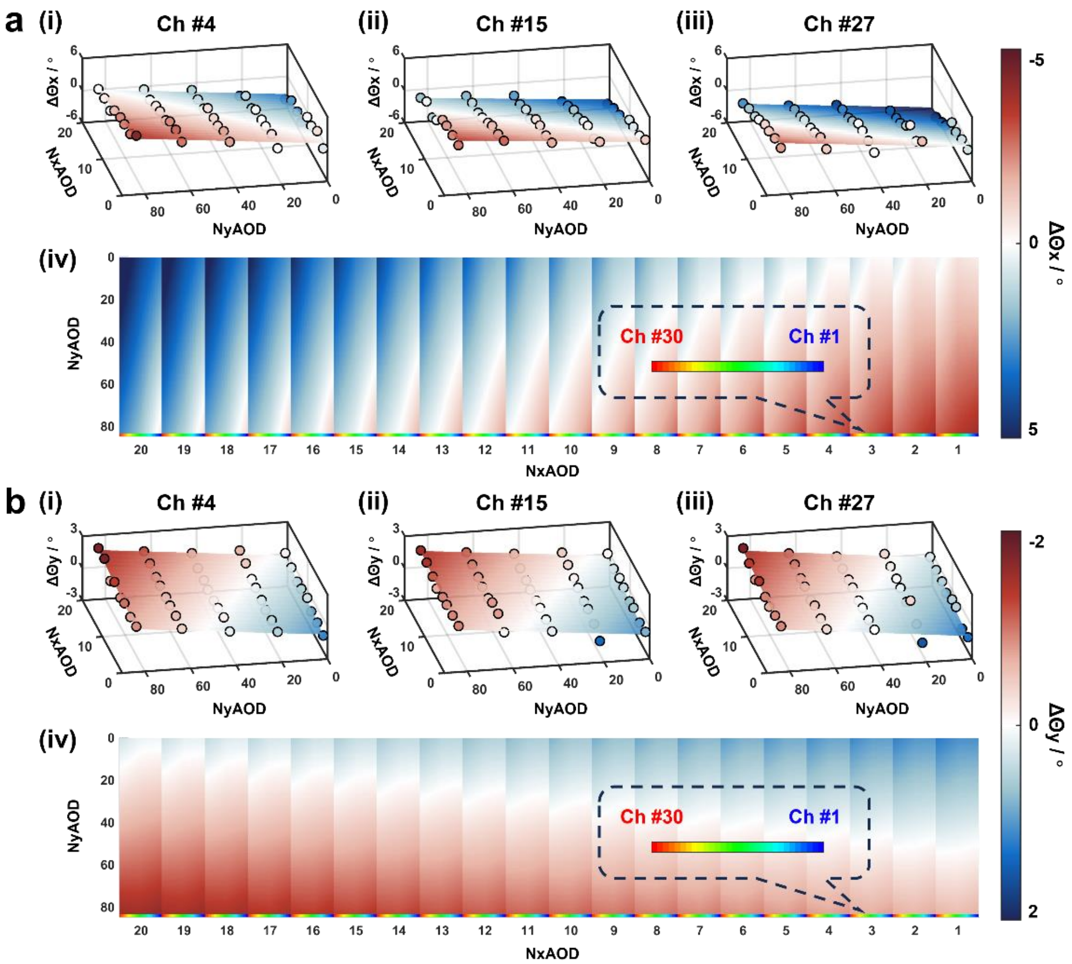

Fig. S5 | Characterization of beam deflection angle deviations. (**a**) $\Delta\Theta_x$ and (**b**) $\Delta\Theta_y$. (i)-(iii) Angular deviations for Ch #4, #15, and #27; (iv) Angular deviations across all scanning points derived from the linear fitting of (i)-(iii). The color bar in the inset indicates that each xAOD scanning position includes 30 spectral scanning points (totaling 20 × 30 = 600 scanning points in the x-direction).

2. Wide-FOV 2D imaging experiment

To characterize the wide-FOV performance of the fabricated AML, we conducted a 2D imaging experiment using a 1D scanning beam. As shown in Fig. S6a, four objects with reflective tape are placed at different positions on the same horizontal plane. The horizontal width of the objects and their center positions on the horizontal plane (x_i, z_i) are indicated in Fig. S6b, corresponding to angle positions of -47.35°, -9.49°, 27.20°, and 45.74°. The left edge angle of object 1 is -50.33°, while the right edge angle of object 4 is 50.84°, resulting in a required FOV of 101.17°.

We fixed yAOD at its center driving frequency of 50MHz and varied xAOD's frequency, enabling spectral-AO cascade 1D beam scanning. This produced a series of horizontal scanning spots at $\Theta_y = 0°$ as depicted in Fig. 3c of the main text, with a theoretical maximum FOV range of [-51.30°, 50.96°], covering the edge FOV of the objects at [-50.33°, 50.84°]. In Fig. S6c, an orange pulse along with the subsequent blue echoes represents a set of spectral scanning data (with N_λ = 30 angular spatial positions). There are 7 such sets of spectral scanning data, corresponding to 7 scanning points of xAOD (scanning towards the negative x-direction), resulting in a total of 7×30 angular positions.

As illustrated in the inset of Fig. S6c, the TOF information is obtained from the time delay between the echoes and the calibrated reference timing (gray dashed line). This allowed us to derive an intensity-distance mapping at 210 angular coordinates. By converting the polar coordinates to Cartesian coordinates, we were able to reconstruct a 2D image resembling the top view of the objects, as shown in Fig. S6d. This confirms that we successfully detected all four objects experimentally, thereby validating our theoretical FOV coverage of the area. Moreover, the spatial positions of the imaged objects closely match the actual measurements (green points and orange lines), further demonstrating the wide-FOV performance of the AML and the ranging capability of the LiDAR system.

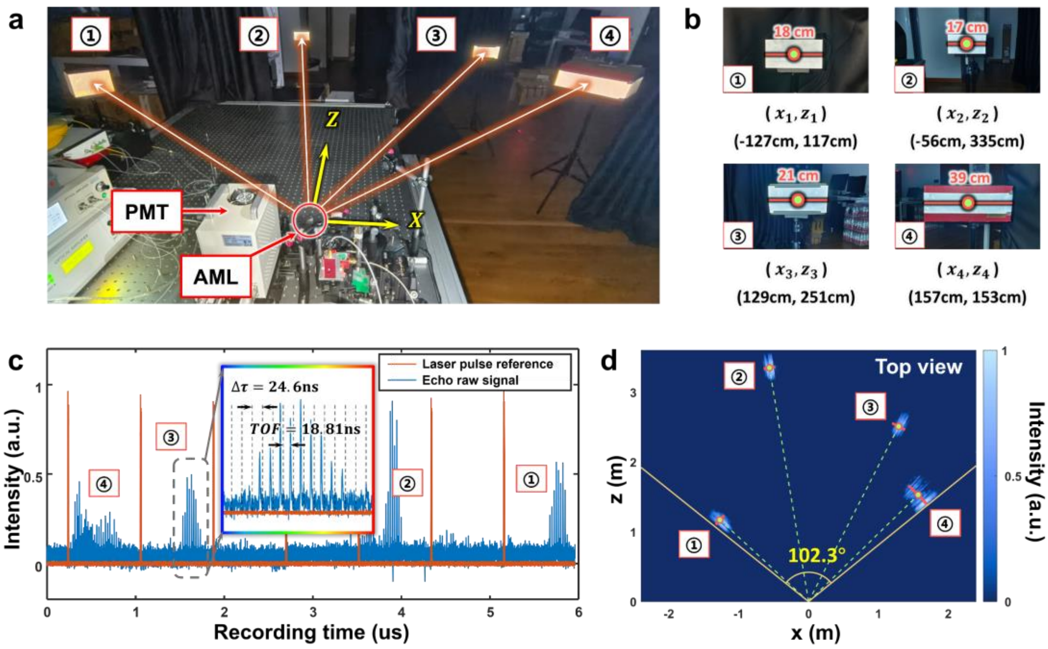

Fig. S6 | Wide-FOV ranging capability. (**a**) Imaging scenario with all objects positioned on the same horizontal plane. (**b**) Four objects covered with reflective tape, with their widths indicated by orange lines and their central positions on the horizontal plane denoted by green dots at coordinates (x_i, z_i). (**c**) Raw echo signal of the scanned objects (blue curve) and reference laser pulse (orange curve) recorded during a single scanning cycle. (**d**) Ranging image of the four objects. Green dashed lines represent the true angular positions calculated from (**b**), while the orange line segments and green dots mark the central positions and widths of the objects. The graph illustrates the system's ability to detect all four objects, achieving a horizontal FOV exceeding 102°.

Our current maximum FOV is not a limit imposed by the AML itself; instead, it is constrained by the periodicity of the meta-atoms, which determines the maximum phase gradient they can provide. However, this periodicity is also limited by the constraints of micro-nano fabrication techniques. Theoretically, we could achieve larger FOV by utilizing a smaller meta-atom periodicity that offers a greater phase gradient.

Supplementary Section 6: Characterization of the beam divergence angle.

To characterize the astigmatism correction capability of the AML for practical beam conditions, we used a CCD (Allied Vision, Goldeye G-130 TEC1, 1280 × 1024 pixels, 5 µm × 5 µm pixel size) to record the intensity distribution of the beam as it propagated downstream of the collimator (COL) (representing the input of the entire optical system), the COL + BG, and the AML (whole system). From these measurements, we fitted the divergence and deflection angles of the beams using the following Gaussian function model:

$$I_{gaussian\_fitted}(x,y) = A\cdot\exp\left(-\frac{(x-x_0)^2}{2\sigma_{\omega x}^{\ 2}} - \frac{(y-y_0)^2}{2\sigma_{\omega y}^{\ 2}}\right) + I_n \quad \text{(S8)}$$

$$\omega_x = 2\sigma_{\omega x}\ ,\ \omega_y = 2\sigma_{\omega y} \quad \text{(S9)}$$

where I_n represents the background noise intensity, (x, y) are the 2D coordinates on the CCD, (x_0, y_0) are the Gaussian beam center positions, and ω_x, ω_y represent the beam waist radii in the x/y directions (the radius at which the intensity falls to e^{-2} of its maximum). The beam divergence angle $\theta_{x,y}$ is calculated by $\boldsymbol{d\omega_{x,y}/dz}$, where z denotes the propagation distance.

Figure S7 shows the beam propagation evolution downstream of the COL. After fitting, the input divergence angles θ_x and θ_y were found to be 0.803 mrad and 0.790 mrad, respectively, indicating an almost perfectly circularly symmetric Gaussian beam.

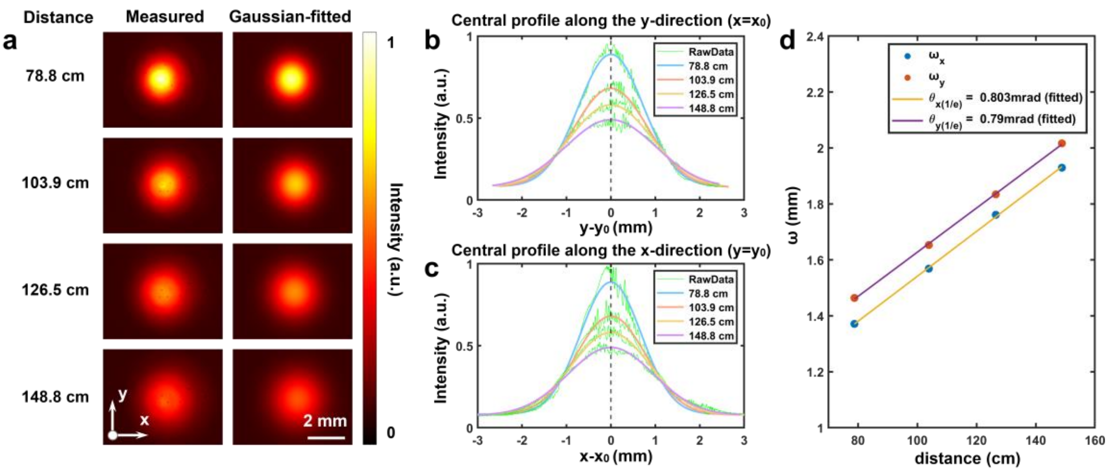

Fig. S7 | Beam propagation evolution after the collimator (COL). (**a**) Beam intensity distributions at different distances downstream of the COL (Left: measured; Right: Gaussian-fitted). (**b**)(**c**) Central intensity profiles of the beam along (**b**) the y-direction ($x = x_0$) and (**c**) the x-direction ($y = y_0$). (**d**) Beam waist radii ω_x, ω_y as functions of propagation distance, and the corresponding divergence angles θ_x, θ_y derived from linear fitting.

Figure S8 shows the beam propagation evolution downstream of the COL and the BG. We fitted the deflection angles Θ induced by grating dispersion based on the variation of the beam's center positions x_0 at different wavelengths (taking the center of the middle wavelength beam as the zero reference, calculated by $d(x_{0\_\lambda i} - x_{0\_\lambda 21})/dz$), as shown in Fig. S8b. Through fitting, the average angular separation between adjacent wavelengths was found to be ~ 0.564 mrad. Additionally, the average beam divergence angles θ_x and θ_y were 2.36 mrad and 0.768 mrad, respectively, indicating significant astigmatic properties.

In comparison, Fig. S9 shows the beam propagation evolution downstream of the AML (whole system). Fig. S9b shows that the average angular separation between adjacent wavelengths is ~ 9.4 mrad. The fitted average beam divergence angles θ_x and θ_y were 11.8 mrad and 10.2 mrad, respectively, with significant suppression of astigmatism.

Moreover, we used the ratio of the deflection angle between adjacent wavelengths to the divergence angle of a single wavelength to describe the relative beam separation:

$$\frac{\overline{\Delta\Theta_{\lambda_i-\lambda_{i+1}}}}{\overline{\theta_x}}(\text{before astigmatism correction}) = \frac{0.564\text{mrad}}{2.36\text{mrad}} = 23.9\% \qquad \text{(S10)}$$

$$\frac{\overline{\Delta\Theta_{\lambda_i-\lambda_{i+1}}}}{\overline{\theta_x}}(\text{after astigmatism correction}) = \frac{9.4\text{mrad}}{11.8\text{mrad}} = 79.7\% \qquad \text{(S11)}$$

It is evident that after the AML corrects the astigmatism, the beam separation between adjacent spectral channels increases (~3.3-fold improvement), which is not achievable with conventional non-astigmatic telescopic systems that simultaneously amplify both the deflection and divergence angles.

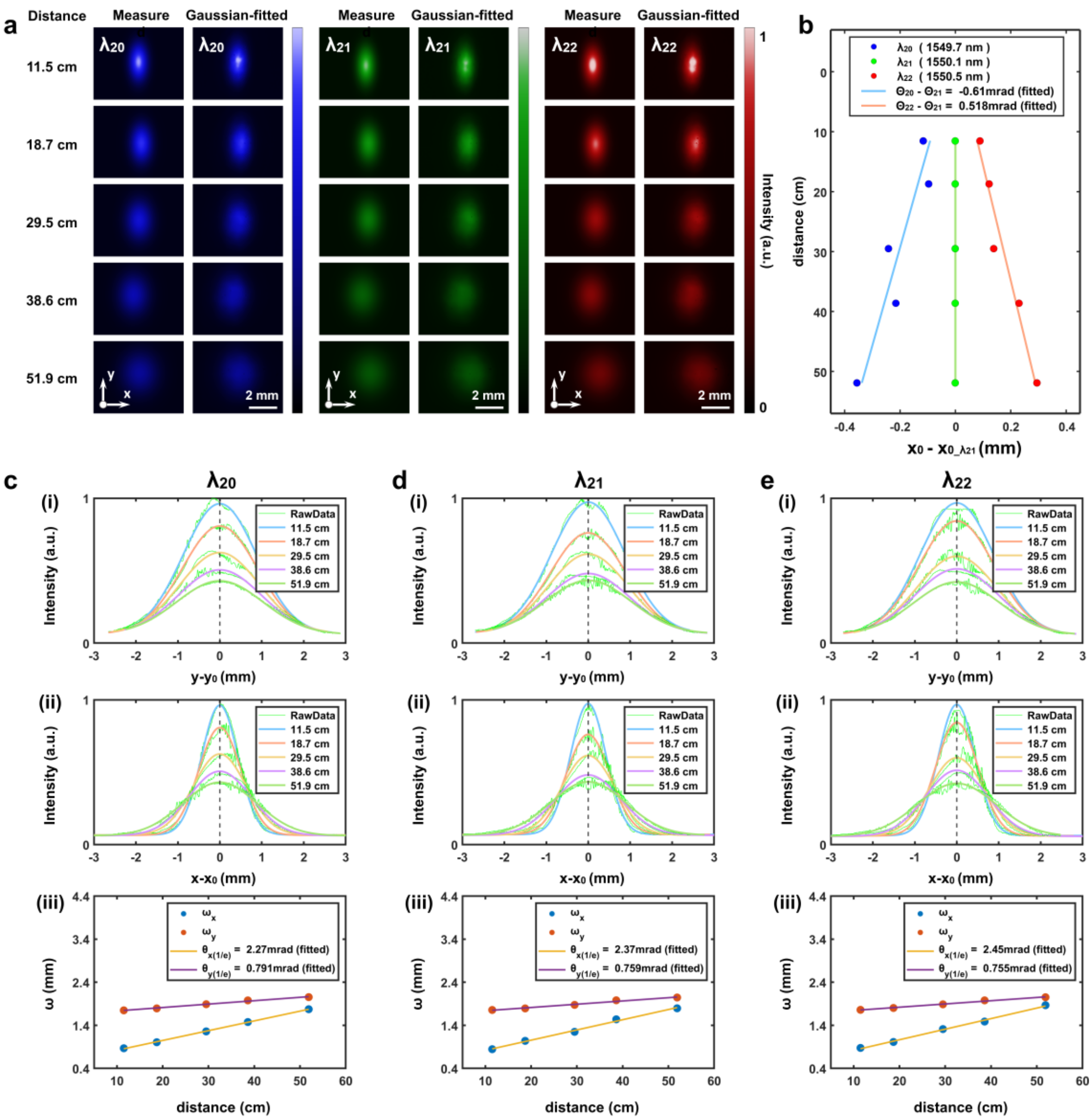

Fig. S8 | Beam propagation evolution after the COL and BG. (a) Beam intensity distributions for three adjacent wavelengths (λ_{20}, λ_{21}, λ_{22}) at different distances downstream of the COL and BG. (**b**) Relative angular deviations of the adjacent wavelength beams obtained from the center positions x_0 of their intensity distributions. (**c**)-(**e**) Central intensity profiles of the beam along (i) the y-direction ($x = x_0$) and (ii) the x-direction ($y = y_0$). (iii) Beam waist radii ω_x, ω_y as functions of propagation distance, and the corresponding divergence angles θ_x, θ_y derived from linear fitting. Panels (**c**), (**d**), and (**e**) correspond to λ_{20}, λ_{21}, λ_{22}, respectively.

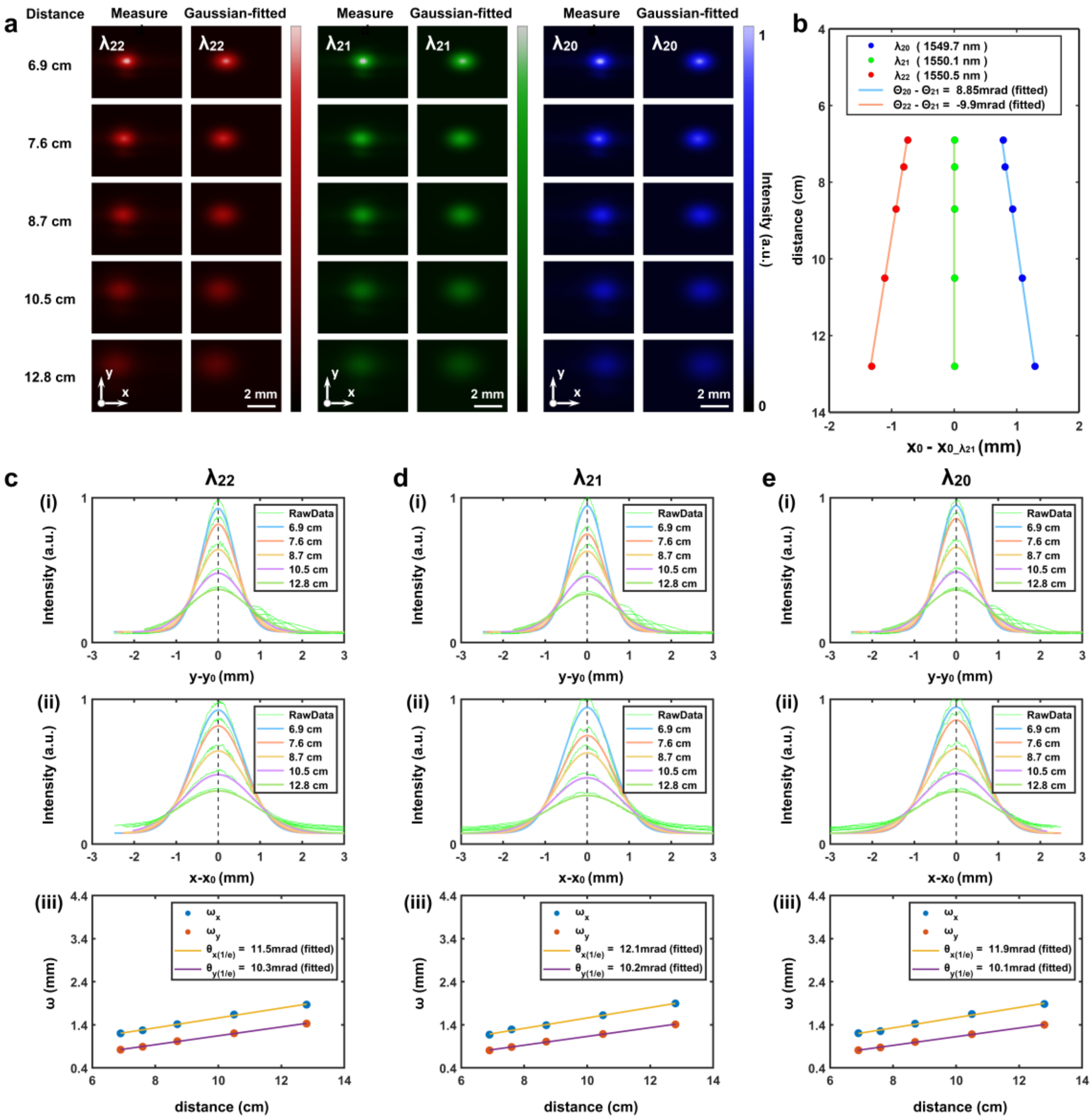

Fig. S9 | Beam propagation evolution after the AML (whole system). (**a**) Beam intensity distributions for three adjacent wavelengths (λ_{20}, λ_{21}, λ_{22}) at different distances downstream of the AML. (**b**) Relative angular deviations of the adjacent wavelength beams obtained from the center positions x_0 of their intensity distributions. (**c**)-(**e**) Central intensity profiles of the beam along (i) the y-direction ($x = x_0$) and (ii) the x-direction ($y = y_0$). (iii) Beam waist radii ω_x, ω_y as functions of propagation distance, and the corresponding divergence angles θ_x, θ_y derived from linear fitting. Panels (**c**), (**d**), and (**e**) correspond to λ_{22}, λ_{21}, λ_{20}, respectively.

Supplementary Section 7: Data processing procedure.

This work employs two data processing methods to reconstruct 3D information from the measured LiDAR raw echo signals, as illustrated in Fig. S10.

The first method directly extracts the TOF corresponding to the echo peak of each pulse to generate a point cloud (Fig. 4 of the main text). As depicted in Fig. S10a, we begin by applying a series of noise-suppression procedures to the raw echoes, including β-fold averaging (if β>1), frequency-domain low-pass filtering, and intensity-threshold-based denoising. Then, we employ a three-point fitting method[7] to further refine the TOF estimation. Once the preliminary point cloud is formed by assigning each TOF to (Θ_x, Θ_y, D), a statistical filtering step (via MATLAB's *pcdenoise* function) removes outliers, yielding a cleaner point cloud reconstruction, as shown in Fig. S10b.

Rather than assigning a single TOF to each pulse, the second method accounts for beam divergence and integrates all echo signals to perform slice-based reconstruction across the entire 3D volume (Fig. 5 of the main text). As depicted in Fig. S10c, subpixel reconstruction integrates the Gaussian intensity distribution of the beams within the pixel grid (Θ_{xm}, Θ_{yn}, D_k). Each pixel's intensity is weighted by contributions from all nearby beams, as defined in the following equation:

$$I_{\text{reconstructed}}(\Theta_{xm},\Theta_{yn},D_k)=\frac{\sum_i\sum_j I(\Theta_{xi},\Theta_{yi},D_k)\cdot\exp\left(-\frac{(\Theta_{xi}-\Theta_{xm})^2}{2\sigma_x^{\,2}}-\frac{(\Theta_{yi}-\Theta_{yn})^2}{2\sigma_y^{\,2}}\right)}{\sum_i\sum_j 1\cdot\exp\left(-\frac{(\Theta_{xi}-\Theta_{xm})^2}{2\sigma_x^{\,2}}-\frac{(\Theta_{yi}-\Theta_{yn})^2}{2\sigma_y^{\,2}}\right)} \quad \text{(S12)}$$

$$\sigma_x=\frac{1}{2}\theta_x\ ,\ \sigma_y=\frac{1}{2}\theta_y \quad \text{(S13)}$$

where I (Θ_{xi}, Θ_{yj}, D_k) denotes the echo signal intensity at the i-th and j-th actual beam scanning positions in the x- and y-directions, respectively, and the k-th distance (corresponding to a specific echo timestamp). Meanwhile, $I_{\text{reconstructed}}$ (Θ_{xm}, Θ_{yn}, D_k) represents the reconstructed intensity at the m/n-th grid position in the x/y-direction, and the k-th distance. The numerator on the right-hand side of Eq. S12 accounts for the combined influence of all nearby beams (Θ_{xi}, Θ_{yj}) on the grid position (Θ_{xm}, Θ_{yn}), while the denominator corrects for the non-uniform distribution of the actual beams. The Gaussian beam's standard deviation, $\sigma_{x,y}$, is defined as half of the divergence angle $\theta_{x,y}$ at which the beam intensity falls to e^{-2} of its maximum.

As shown in Fig. S10c(iii), the final reconstructed intensity $I_{\text{reconstructed}}$ (Θ_x, Θ_y, D) can be visualized as a series of distance slices, revealing fine spatial details that are difficult to resolve using direct point-cloud processing (Fig. 5 in the main text).

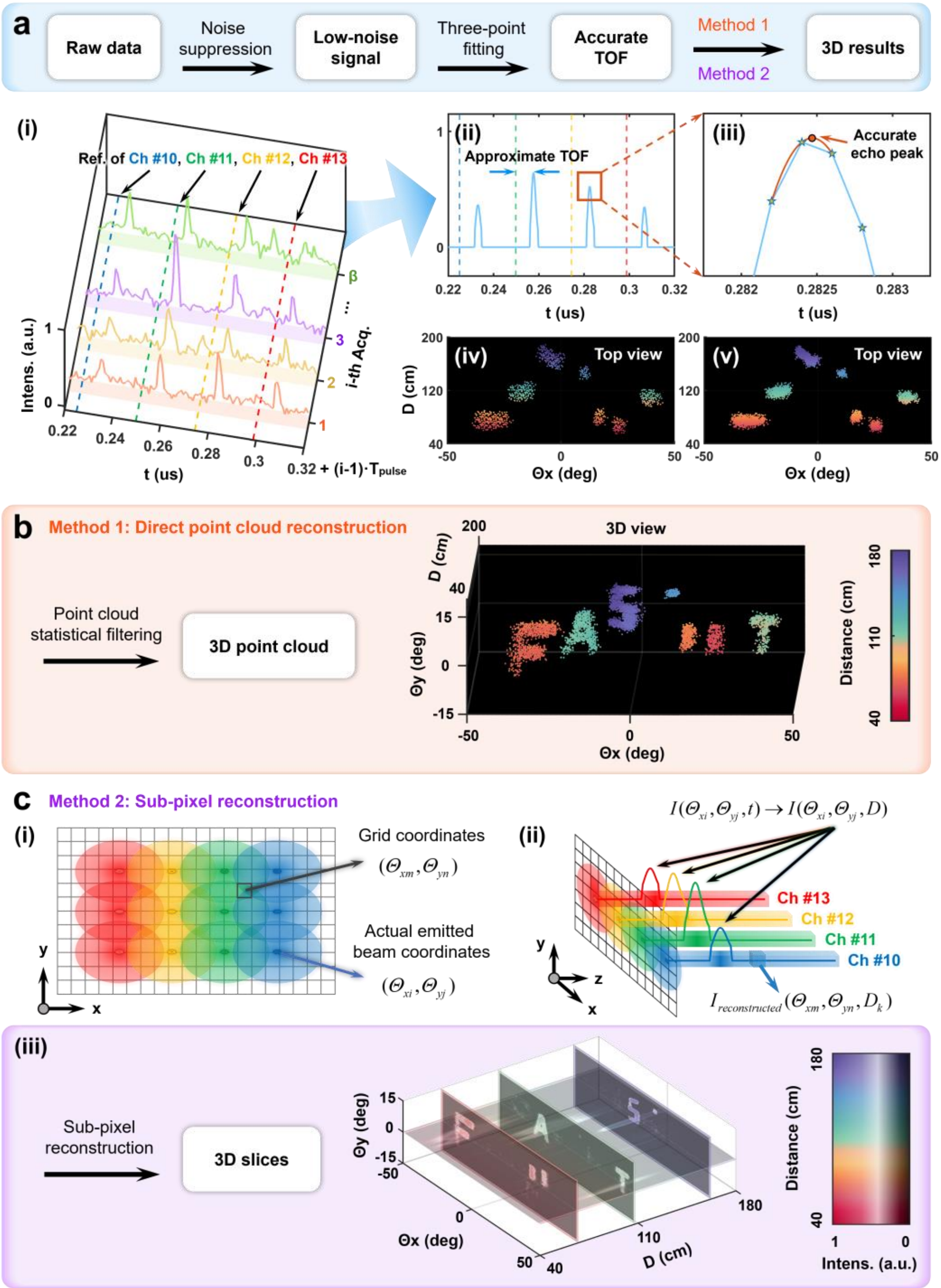

Fig. S10 | Data processing for 3D reconstruction. (**a**) Flowchart of the raw echo data processing procedure: (i) β repeated acquisitions at a single scanning position. (ii) Apply multiple averaging steps, frequency-domain filtering, and threshold-based denoising to obtain a low-noise signal. (iii) Use three-point fitting to extract more accurate TOF. (iv)&(v) Top view images of the reconstruction results before and after three-point fitting, highlighting a substantial improvement in ranging resolution. (**b**) Method 1: Direct point cloud reconstruction to generate the final 3D point cloud image. (**c**) Method 2: Subpixel reconstruction. (i) In method 1, every pulse is mapped to a point (Θ_{xi}, Θ_{yj}, D_{peak}) based on the timestamp of the echo peak. In contrast, subpixel reconstruction accounts for beam divergence: within the pixel grid (Θ_{xm}, Θ_{yn}), the intensity is no longer binary ("1 or 0") but is modulated by the Gaussian distribution of surrounding beams. (ii) From each actual emitted beam, the entire echo waveform is used to obtain I (Θ_{xi}, Θ_{yj}, D), enabling further 3D reconstruction of $I_{\text{reconstructed}}$ (Θ_{xm}, Θ_{yn}, D_k) for every grid location. (iii) The resulting $I_{\text{reconstructed}}$ can be visualized as multiple slice views, revealing the intensity distribution at various distances.

Supplementary Section 8: Discussion on ranging resolution.

The achieved ranging/depth resolution is determined by the timing precision of the system, which is influenced by several factors: (i) the stability of the laser source pulse period, (ii) the pulse width of the laser source, (iii) pulse broadening introduced by modulation devices, (iv) the inherent timing jitter of the detector, and (v) the sampling rate of the digitizer. In our experimental setup, the primary contributors to timing error are factors (iv) and (v).

On the one hand, the intrinsic error of the photomultiplier tube (PMT) arises from the transit time caused by its multi-stage amplification mechanism. When a single photon strikes the PMT, the photocathode converts it into photoelectrons, which are then multiplied through a series of dynodes before reaching the anode. The total transit time of the electron group depends on each incident photon, resulting in a dispersion known as transit time spread (TTS). According to the manufacturer's specifications, the PMT (HAMAMATSU, H10330C-75) has a TTS of 0.4 ns. On the other hand, in the experiments presented in Figs. 4 and 5 of the main text, we utilize a data acquisition card (Teledyne, ADQ7DC) as the digitizer, which records data at a sampling rate of 5 GS/s, yielding a time resolution of 0.2 ns.

As a result, the overall ranging resolution of our system is primarily constrained by the PMT's TTS of 0.4 ns, which corresponds to a theoretical ranging resolution of ~ 6 cm. However, as shown in Fig. 4b of the main text, we actually achieve an improved ranging standard deviation σ of ~ 3 cm. This enhancement is primarily attributed to the use of three-point fitting, which enables sub-sample TOF estimation. In addition, the measured σ reflects the statistical variation of echo returns from a relatively uniform target surface, rather than the intrinsic timing jitter associated with individual photon detection events.

Supplementary Section 9: Power loss analysis & discussion on long-range detection.

As shown in Fig. S11, the primary power losses in our system occur at the AOD and the AML, mainly due to fabrication defects. Consequently, the actual effective power at the transmitter end is only a few milliwatts, limiting the range of our imaging experiments, which were conducted at distances of <3.4 m. According to the inverse square law governing the relationship between received scattered power and detection distance, achieving longer-range detection requires addressing the challenge of weak echo signals. This can be approached through several strategies: (i) increasing the transmission power (with attention to the device's damage threshold); (ii) further suppressing angular divergence; (iii) employing more sensitive detectors; and (iv) performing frequency up-conversion on the echo signals to shift them into the visible spectrum, aligning within the high responsivity range of mature silicon-based photodetectors, thus improving detection efficiency[8, 9].

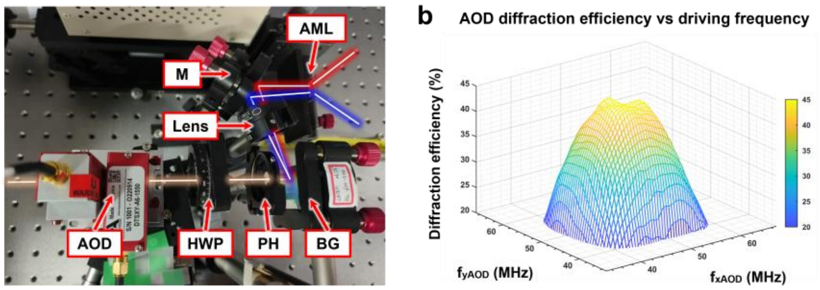

c

	HWP	BG	Lens	M	ML(1 order)	ML(0 order)	ML(Total)
T_{min}	97.1%	69.3%	97.4%	97.0%	32.3%	13.3%	46.2%
T_{max}	99.2%	88.9%	99.0%	99.9%	51.5%	20.6%	65.2%
$\bar{T}$ (Loss)	98.80% (0.05 dB)	83.02% (0.81 dB)	92.62% (0.33 dB)	98.14% (0.08 dB)	40.12% (3.97 dB)	15.18%	55.30%

Fig. S11 | Power loss analysis. (a) Photograph of the optical system at the transmitter end, after the COL. (**b**) Diffraction efficiency of the dual-axis AOD. (**c**) Transmittance/diffraction efficiency of other optical elements (including a total of 50 measurements evenly distributed across the entire FOV, with the last row representing the average result after removing outliers).

References

1. Jiang Y, Karpf S, Jalali B. Time-stretch LiDAR as a spectrally scanned time-of-flight ranging camera. *Nature photonics* **14**, 14-18 (2020).
2. Juliano Martins R, Marinov E, Youssef MAB, Kyrou C, Joubert M*, et al.* Metasurface-enhanced light detection and ranging technology. *Nature Communications* **13**, 5724 (2022).
3. Zang Z, Li Z, Luo Y, Han Y, Li H*, et al.* Ultrafast parallel single-pixel LiDAR with all-optical spectro-temporal encoding. *APL Photonics* **7**, 046102 (2022).
4. Qian R, Zhou KC, Zhang J, Viehland C, Dhalla A-H*, et al.* Video-rate high-precision time-frequency multiplexed 3D coherent ranging. *Nature communications* **13**, 1476 (2022).
5. Chen R, Shu H, Shen B, Chang L, Xie W*, et al.* Breaking the temporal and frequency congestion of LiDAR by parallel chaos. *Nature Photonics* **17**, 306-314 (2023).
6. Lukashchuk A, Riemensberger J, Karpov M, Liu J, Kippenberg TJ. Dual chirped microcomb based parallel ranging at megapixel-line rates. *Nature Communications* **13**, 3280 (2022).
7. Wang J, Lu Z, Wang W, Zhang F, Chen J*, et al.* Long-distance ranging with high precision using a soliton microcomb. *Photonics Research* **8**, 1964-1972 (2020).
8. Albota MA, Wong FN. Efficient single-photon counting at 1.55 µm by means of frequency upconversion. *Optics letters* **29**, 1449-1451 (2004).
9. Rehain P, Sua YM, Zhu S, Dickson I, Muthuswamy B*, et al.* Noise-tolerant single photon sensitive three-dimensional imager. *Nature communications* **11**, 921 (2020).